Strain in silicon nanowire beams

Ferran Ureña, Sarah H. Olsen, Lidija Šiller, Umesh Bhaskar, Thomas Pardoen et al.

Citation: J. Appl. Phys. **112**, 114506 (2012); doi: 10.1063/1.4765025
View online: http://dx.doi.org/10.1063/1.4765025
View Table of Contents: http://jap.aip.org/resource/1/JAPIAU/v112/i11
Published by the American Institute of Physics.

Strain in silicon nanowire beams

Ferran Ureña,[1,a)] Sarah H. Olsen,[1] Lidija Šiller,[2] Umesh Bhaskar,[3] Thomas Pardoen,[4] and Jean-Pierre Raskin[3]
[1]*School of Electrical and Electronic Engineering. Newcastle University, United Kingdom*
[2]*School of Chemical Engineering and Advanced Materials. Newcastle University, United Kingdom*
[3]*Université catholique de Louvain, Institute of Information and Communication Technologies, Electronics and Applied Mathematics (ICTEAM), Louvain-la-Neuve, Belgium*
[4]*Université catholique de Louvain, Institute of Mechanics, Materials and Civil Engineering (IMMC), Louvain-la-Neuve, Belgium*

(Received 24 July 2012; accepted 12 October 2012; published online 4 December 2012)

In this work, strain in silicon free standing beams loaded in uniaxial tension is experimentally and theoretically investigated for strain values ranging from 0 to 3.6%. The fabrication method allows multiple geometries (and thus strain values) to be processed simultaneously on the same wafer while being studied independently. An excellent agreement of strain determined by two non-destructive characterization techniques, Raman spectroscopy and mechanical displacement using scanning electron microscopy (SEM) markers, is found for all the sample lengths and widths. The measured data also show good agreement with theoretical predictions of strain based upon continuum mechanical considerations, giving validity to both measurement techniques for the entire range of strain values. The dependence of Young's modulus and fracture strain on size has also been analyzed. The Young's modulus is determined using SEM and compared with that obtained by resonance-based methods. Both methods produced a Young's modulus value close to that of bulk silicon with values obtained by resonance-based methods being slightly lower. Fracture strain is analyzed in 40 sets of samples with different beam geometries, yielding values up to 3.6%. The increase in fracture strain with decreasing beam width is compared with previous reports. Finally, the role of the surface on the mechanical properties is analyzed using UV and visible lasers having different penetration depths in silicon. The observed dependence of Raman shift on laser wavelength is used to assess the thermal conductivity of deformed silicon. © *2012 American Institute of Physics*. [http://dx.doi.org/10.1063/1.4765025]

I. INTRODUCTION

Suspended silicon beams and nanowires are being widely used in micro- and nano-electromechanical systems (MEMS and NEMS) and in nanowire gate-all-around (GAA) transistors. The superior surface-to-volume ratio of these sub-micrometer dimension structures compared with their macro counterparts makes them highly sensitive to chemical and biological detection and consequently very attractive in fabricating and developing MEMS based sensors.[1–3] Likewise, nanowire gate-all-around devices exhibit superior electrostatic control of the gate compared with planar devices, which results in improved performance.[4,5]

Stress engineering is used in MEMS and NEMS for fabricating and developing piezoresistive based sensors, e.g., pressure and force sensors.[6] In microelectronics, compressive and tensile stresses increase carrier mobility in pMOS and nMOS transistors, respectively.[7–9] However, common problems associated with undesirable or excessive mechanical stresses are also a source of many reliability issues.[10,11] Precise knowledge of mechanical properties such as Young's modulus, fracture strain, and fracture stress is needed. The mechanical, thermal, and electrical properties of bulk silicon are well known and have been extensively studied.[12] However, they change significantly at the nanoscale.[13–15] This is because the surface-to-volume ratio significantly increases and the surface atoms start to play a more important role in the physical properties of the material. In solids, during the process of creating a new surface, the free energy increases.[16] The charge distribution at the surface and in the bulk is different due to the absence of atoms above the free surface.[17] As a result, the surface atoms rearrange in order to minimize their positional energy.[16] This surface reconstruction is considered to be the leading mechanism for the observed change in some physical properties in silicon at the nanoscale, for example elasticity and thermal conductivity.[18,19] Thus, with devices well into the nanometer regime, a fundamental understanding of the mechanical properties in silicon suspended beams and nanowires is crucial.

Numerous testing methods have been previously used to perform mechanical tests in silicon free-standing beams replicating nanowires. Buckling and bending are common dedicated methods. In general, they use an atomic force microscope (AFM) tip to deform a cantilever or nanowire and thereafter measure the exerted force.[20–22] Other techniques use singular mechanisms to supply the needed deformation force, for example by inserting a material between cantilevers or by using a polymer spun over the base of an array of nanowires pillars to create a contraction force which deforms the nanowires.[23,24] In these techniques, it can be difficult to precisely control the exerted force. Often a probe for the specimen manipulation is required.[25] Methods based on buckling and bending are also

[a)]Author to whom correspondence should be addressed. Electronic mail: ferran.urena@newcastle.ac.uk.

frequently complicated by the non-linear analysis associated with the specimen deformation. Further challenges arise from the difficulty in obtaining large and uniform ranges of strain with precision, especially in long free-standing beams which are required for generating high values of strain. In silicon high strain values are necessary to maximize the potential of the MEMS and NEMS devices.

Tensile testing machines provide a very direct stress-strain measurement and the capability of probing high values of stress. However, the tensile testing stages developed often have complex designs which can complicate the stress-strain analysis.[26–28] Problems derived from external loading such as sample manipulation, gripping issues, and misalignment are also encountered.[29–31] Furthermore, most tensile testing machines require an electrical based actuator to pull the sample specimen, which generally involves an additional power supply and high precision.

A large number of characterization techniques are capable of measuring strain in silicon structures, including x-ray diffraction (XRD),[32] transmission electron microscopy (TEM), and convergent beam electron diffraction (CBED).[33–35] However, not all of those are suitable for nanoscale analysis. XRD is a non-destructive technique which requires limited effort in sample preparation and can directly measure strain from a crystalline lattice, but its spatial resolution is limited to several micrometers and requires large sample areas. TEM and CBED provide high resolution measurements but require time-consuming destructive sample preparation. Raman spectroscopy is also widely used for strain characterization. It is non-destructive and does not require sample preparation. It can readily achieve spatial resolution below 1 μm, while measuring stress levels down to 25 MPa.[36] In this paper, we use Raman spectroscopy to characterize strain in arrays of silicon beams in a wide range of geometries under uniaxial tensile stress along the [110] direction. The induced strain is varied and controlled by using different beam geometries of a large number of structures fabricated on the same chip. This on-chip tensile-testing technique was recently reported by Gravier *et al.*[37] for measuring the mechanical properties of micro- and nanometer-thick films while avoiding the issues described above. The method has previously been successfully applied to test the mechanical properties of aluminium, palladium, and polysilicon thin films.[37–39] In this work, strain values ranging from 0 to 3.6%, equivalent to an applied stress of ~6 GPa, have been investigated in silicon. Raman spectroscopy and scanning electron microscopy (SEM) are used to characterize strain, and the measured results are compared with analytical calculations. The impact of the surface-to-volume ratio on the mechanical properties of silicon is studied by analyzing the changes in Young's modulus and fracture strain. Surface effects are analyzed with Raman spectroscopy by using a UV laser characterized by a low penetration depth and comparing results with a visible laser which senses the whole thickness of the silicon samples. The discrepancy between the Raman shifts measured using the UV and visible lasers is used to investigate the thermal conductivity in strained silicon.

The paper is organized as follows. Section II describes the fabrication details and measurement conditions. Section III A presents the strain data extracted using Raman shifts and SEM images of released microstructures and discusses the accuracy of the analysis. The experimental data are compared with analytical calculations, and the range of elasticity in silicon is evaluated alongside other experimental and theoretical work. Section III B addresses the variation in Young's modulus and fracture strain with beam geometry. The role of the surface in the size dependent physics is analyzed in Sec. III C. The impact of strain on the thermal conductivity of silicon is discussed in Sec. III D. Finally, the main conclusions are summarized in Sec. IV.

II. EXPERIMENTS

The samples consist of six arrays of silicon beams having beam widths of 1, 2, 4, 6, 8, and 10 μm. The beams are under tensile stress along the [110] direction. Each array is composed of thirty beams with lengths varying between 3 and 1300 μm and a constant thickness of 200 nm. The induced stress is provided by a silicon-nitride beam (actuator) attached to the silicon sample. The actuator widths are 10 and 15 μm and the thickness is 400 nm. The length of the actuator is varied between 175 and 1988 μm. The total length of the actuator and sample is kept constant and four different configurations with lengths of 500, 1000, 1500, and 2000 μm were fabricated (Fig. 1). Thus, the total number of samples is $6 \times 30 \times 2 \times 4 = 1440$. The large number of samples has allowed us to investigate the size effects and surface effects on the mechanical properties of strained silicon for a large range of geometries and stress values.

Fig. 2 shows the complete fabrication process. It starts with a standard (100) SOI (silicon-on-insulator) wafer with a 400 nm-thick top silicon film. An oxide layer is thermally grown above the silicon film and thereafter used as a mask for patterning the silicon into beams. After sample patterning using plasma etching, a second oxide layer is thermally grown and a window opened where the actuator contacts the sample. A 400 nm-thick silicon nitride layer is then deposited by low pressure chemical vapor deposition at high temperature (800 °C) and patterned for making the actuator. Finally, the sample (Si) and actuator (Si_3N_4) are released by etching the silicon dioxide sacrificial layer with hydrofluoric acid (HF). A critical point drying process completes this step for

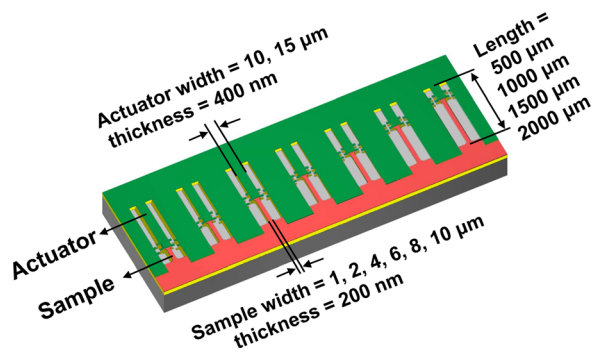

FIG. 1. The array of microstructures used in this work. Every array consists of 30 samples with lengths ranging from 3 to 1300 μm, six different widths (1 – 10 μm), and two different actuator widths (10 and 15 μm). The thickness of the samples and actuators are 200 and 400 nm, respectively. The total length, i.e., sample and actuator, is also varied between 500 and 2000 μm.

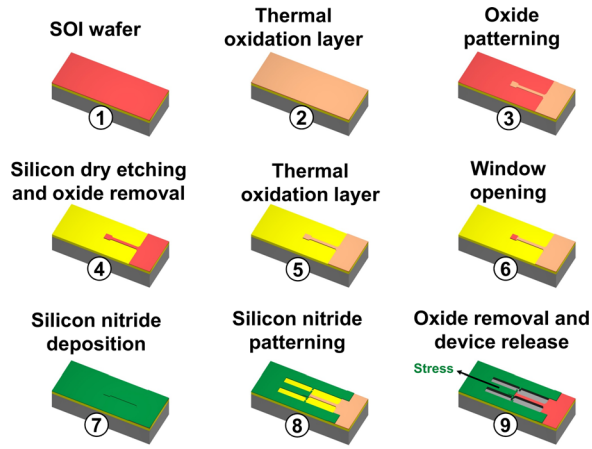

FIG. 2. The fabrication process flow for the MEMS-based silicon beams. An induced stress due to the contraction of the actuator appears in the silicon sample beam after the final release process.

avoiding stiction with the substrate. As a result of the silicon nitride high deposition temperature and the difference in thermal expansion coefficients between silicon nitride ($\alpha \sim 6 \cdot 10^{-6}\ K^{-1}$) and silicon ($\alpha \sim 2.3 \cdot 10^{-6}\ K^{-1}$),[37] the silicon nitride undergoes internal stress relaxation after the final HF release. This induces a tensile stress in the silicon sample. Additional fabrication details can be found in Ref. 37.

In order to determine strain in the samples by SEM, a pair of cursors was fabricated alongside the silicon beams (Fig. 3(a)). One cursor is positioned at the actuator side (mobile cursor) and the other is positioned at the substrate sidewalls (fixed cursor). The displacement between the mobile and fixed cursors (inset in Fig. 3(a)) is directly measured by SEM inspection and converted to strain ε using the logarithmic norm (true strain). This logarithmic norm is generally used in large deformation behavior.[40] Strain is given by

$$\varepsilon = ln\left(\frac{L_0 + u}{L_0}\right), \quad (1)$$

where L_0 is the initial sample length before the device release (step 8 in Fig. 2) and u is the mobile cursor displacement after the device release (step 9 in Fig. 2). In order to minimize the error in the strain determination, additional pairs of cursors per sample (four in the present structures) can be implemented and the resulting displacements averaged (Fig. 3(b)). The accuracy for the SEM measurements is estimated to be 50 nm.

Assuming silicon in the elastic regime and uniaxial stress along the [110] direction, strain is converted to stress using Hooke's law:

$$\sigma = \varepsilon E_{110}. \quad (2)$$

Here, σ and ε are the uniaxial stress and strain, respectively, along the [110] direction, and E_{110} is the Young's modulus of bulk silicon for the [110] direction ($E_{110} = 169$ GPa).[41]

Raman spectroscopy was used to analyze strain in the silicon beams. A laser beam is focused onto the sample which generates an energy transfer between the incident photons and the sample, i.e., phonons. The difference in frequency between the incident and scattered light results in a Raman spectrum relating to the phonon energy with a characteristic peak centered at $\sim 520\ cm^{-1}$ for unstressed silicon (Fig. 4).[36] In this work, we have used the silicon substrate as the reference to calibrate the peak position. After calibration, the peak position was found to be located at $520.7\ cm^{-1}$. When stress is applied, the peak shifts towards a lower Raman frequency for tensile stress and a higher Raman frequency for compressive stress. In both cases the difference in peak position for unstressed and stressed samples relates

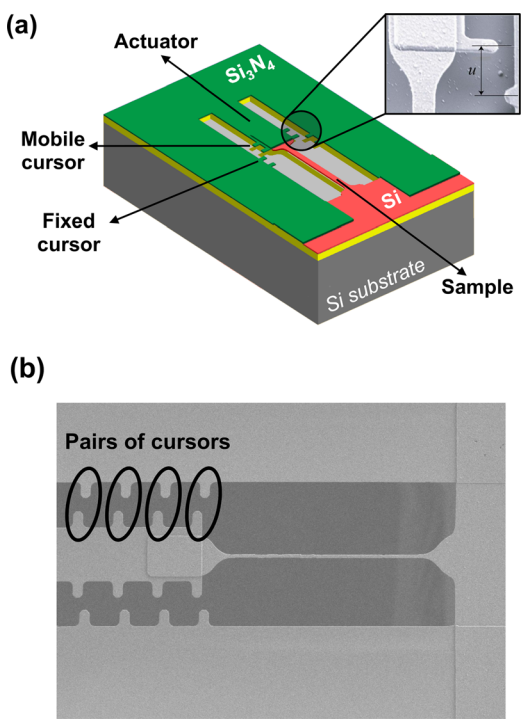

FIG. 3. (a) Mobile and fixed cursors attached to the actuator and silicon nitride sidewalls, respectively, allow accurate SEM measurements of the displacement u (inset); (b) SEM micrograph of a sample showing four pairs of cursors. Multiple cursors are used to minimize error in strain estimated by SEM measurements.

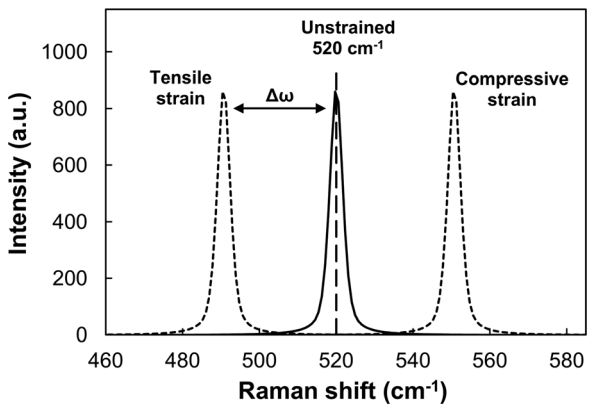

FIG. 4. Typical Raman spectra in silicon. In the absence of stress, silicon exhibits a major peak centered at $\sim 520\ cm^{-1}$. Tensile strain will cause a peak shift towards lower frequency values whereas compressive strain will shift the peak position to higher frequency values.

to the applied stress (Fig. 4).[36] The Raman measurements were performed in backscattering configuration using a commercial LabRam HR 800 confocal laser system with a high numerical aperture (0.9). A visible laser with wavelength $\lambda = 458$ nm and penetration depth ~300 nm[42] was used to characterize strain in the bulk of the silicon samples and a UV laser with wavelength $\lambda = 364$ nm and penetration depth ~15 nm[42] was used to analyze strain near the surface.

For each sample, the laser was focused at three locations near the centre of the beam length, with each measurement separated by 1 μm. Each measurement consisted of 3 accumulations and an integration time of 10 seconds per accumulation in order to optimize measurement accuracy. The Raman information presented for each sample corresponds to the median of the three measurements. For the subsequent analysis, each peak on the Raman spectra was deconvolved using a Gaussian-Lorentzian distribution to determine the peak position and thus strain. The deconvolution process is less accurate for peaks located near the silicon substrate peak (520.7 cm^{-1}) as the high intensity of the substrate peak can mask the other peaks. The maximum difference in peak deconvolution between the three measurements at each location was found to be ~0.33 cm^{-1}, corresponding to the samples with the smallest strain (peak position ~520.7 cm^{-1}). For the samples with higher stress levels, the peak position is clearly resolved and the error in peak position is smaller (~0.05 cm^{-1}, which corresponds to ~26 MPa stress). The error bars for the measurements are very small and are therefore not presented in the figures.

III. RESULTS AND DISCUSSION

A. Elastic strain measurements

The strain and stress induced in the beam can be theoretically deduced from force equilibrium conditions between the actuator and sample beam. Figure 5 compares the structure deformations and force equilibrium involved before and after the sacrificial oxide removal during device fabrication. Figure 5(a) shows the expected deformation which will be experienced by the actuator with no attached sample after the sacrificial oxide etching. Following release, the actuator is free to contract by an amount u_{free} due to its internal stress relaxation. In contrast, the loaded actuator in Fig. 5(b) can only contract by an amount u smaller than u_{free}. Thus, assuming the actuator has a Young's modulus E_a and a cross section S_a, the load condition can be expressed by[37]

$$F = E_a\ S_a \left(\frac{u_{free}}{L_{a0}^{free}} - \frac{u}{L_{a0}} \right) , \tag{3}$$

where L_{a0} and L_{a0}^{free} represent the actuator length with and without the load, respectively, before release. The value $\frac{u_{free}}{L_{a0}^{free}} = \varepsilon_a^{mis}$ represents the mismatch strain of a free actuator (i.e., without an attached sample beam) and is obtained by measuring the cursor positions via SEM images inspection. In our case, $\varepsilon_a^{mis} = 0.00324$.

Using Eq. (3), for the sample beam:

$$F = E\ S \left(\frac{u}{L_0} \right) , \tag{4}$$

where E, S, and L_0 represent the Young's modulus, cross section, and initial length, respectively, before release of the silicon beam. Mismatch strain is not considered since the silicon sample is produced from blanket SOI.[43] Combining Eqs. (3) and (4) to enforce equilibrium, the contracted amount u is estimated as

$$u = \frac{\varepsilon_a^{mis}}{r\frac{1}{L_0} + \frac{1}{L_{a0}}} , \tag{5}$$

where r has been defined as $r = \frac{E}{E_a}\frac{S}{S_a}$.

SEM measurements were carried out to determine strain by direct inspection of the displacement u of the attached cursors. The cursor displacement is compared with the estimated values extracted from the theoretical analysis assuming $E = 169$ GPa and $E_a = 240$ GPa (measured by nanoindentation[44]). Figure 6 shows a comparison of SEM and theoretical estimates of the cursor displacement for 1 μm-wide samples with beam lengths in the range 160 to 1300 μm. There is an excellent agreement between SEM and theory. The maximum observed difference is 0.14 μm (~0.08% strain) and the average difference is 0.07 μm (~0.04% strain). This validates the on-chip testing structures as a suitable method to obtain specific values of strain within a large and uniform range of sample lengths.

Displacement values from SEM cursor measurements were converted to strain using Eq. (1). Figure 7 shows the variation in strain for three beam widths (1, 2, and 4 μm) with length L_0 (before release). There is a general $1/L_0$ dependency in the measured values of strain, as expected from Eq. (1). At short lengths, u and L_0 values become similar in magnitude and the resultant strain significantly increases.

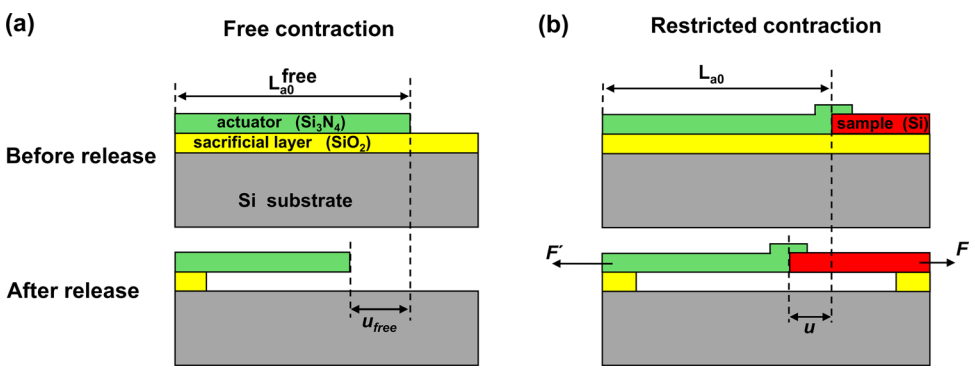

FIG. 5. Schematic showing how the actuator contracts. (a) Actuator is free to contract, i.e., with no attached sample. (b) Actuator is restricted by an attached sample. The actuator deformation u with the attached load is smaller than that of the free actuator u_{free}. Due to the actuator contraction after release, a tensile stress (F-F') is induced along the silicon sample.

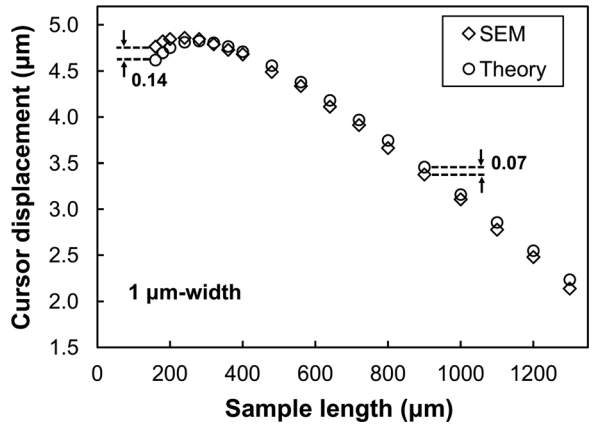

FIG. 6. SEM measurements and theoretical calculations of the cursor displacement u, representing strain (Fig. 3). There is an excellent agreement between theory and SEM measurements.

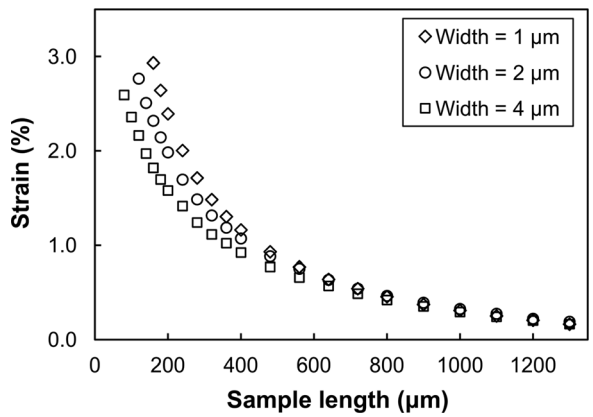

FIG. 7. The strain variation with sample length obtained from direct SEM measurements of cursor displacement. There is a $1/L_0$ dependency in the measured values of strain. At short lengths, both u and L_0 values become similar in magnitude and the resultant strain increases significantly. The measured strain for a given length and thickness becomes smaller for the wider samples as a result of smaller applied stresses.

The increase is more pronounced for the 1 μm-wide samples than for the 2 and 4 μm-wide samples. This is because for a given length and thickness the 1 μm-wide beams have a higher applied stress due to the inverse relationship between stress and cross-section ($\sigma = F/S$).

Raman data were converted to strain to compare with the cursor measurements and analytical estimates of strain. Raman measurements can be affected by sample heating from the irradiating laser.[45,46] Using low laser power circumvents heating effects, however higher laser powers increase the Raman spectra peak intensity and aids accurate identification of peak position. To determine the maximum laser power that could be delivered to the sample before data interpretation becomes erroneous through heating effects, preliminary tests were undertaken. The effects of sample heating were considered for the 1 and 4 μm-wide samples by using different power attenuation filters. By changing the filters the power delivered to the sample is varied from 1 to 100%. The resulting Raman peak is shown in Fig. 8. For the visible radiation, there is no Raman peak shift observed for delivered laser powers below 30 and 200 μW for the 1 μm- and 4 μm-wide

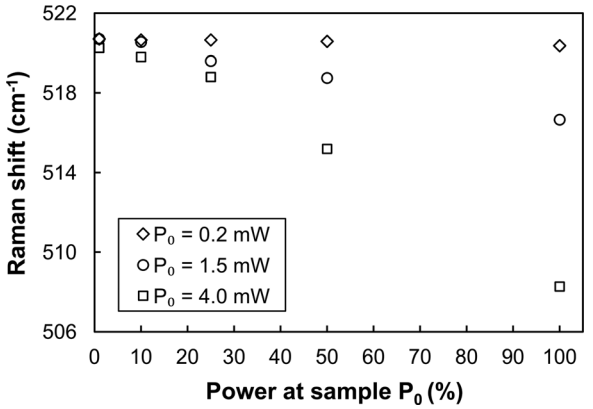

FIG. 8. Raman power tests on 4 μm-wide samples using a visible laser ($\lambda = 458$ nm). Sample delivered powers (P_o) higher than 0.2 mW can introduce shifts in the Raman peak position due to laser sample heating rather than strain. For 1 μm-wide samples P_o must be reduced below 0.03 mW.

samples, respectively, due to a bigger heat evacuation cross-section (Fig. 8). In order to avoid any heating, the delivered power was kept under 30 μW for all the samples. For the UV radiation, the maximum delivered power could not be measured directly. In order to accurately identify peak positions, a minimum attenuation filter of 10% on the UV laser was necessary. Compared with the visible radiation, an additional Raman peak shift due to sample heating is observed. This is 0.05 cm^{-1} for the 4 μm-wide samples and 0.17 cm^{-1} for the 1 μm-wide samples.

The evolution of the Raman frequency peak with the sample length for the visible radiation ($\lambda = 458$ nm) in the 4 μm-wide samples is depicted in Fig. 9. There is a progressive down-shift towards lower frequencies at shorter sample lengths. This corresponds to an increase in the applied tensile stress due to longer actuator lengths and agrees with the trends in strain observed by analytical and SEM cursor displacement methods (Fig. 3(b)).

Figure 10(a) shows the variation in Raman shift with the beam length for the 4 μm-wide samples and lengths ranging from 60 to 1300 μm. Raman shifts are converted to strain using the phonon deformation potentials of Anastassakis

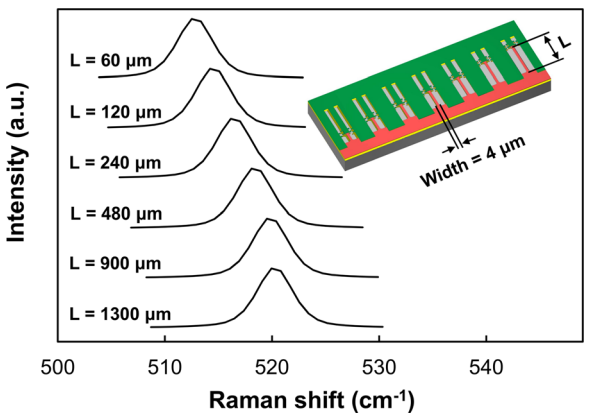

FIG. 9. Raman spectra for varying sample lengths. There is a progressive downshift of the Raman peak position at shorter sample lengths (longer actuator lengths) due to the proportional increase in applied stress with the actuator length.

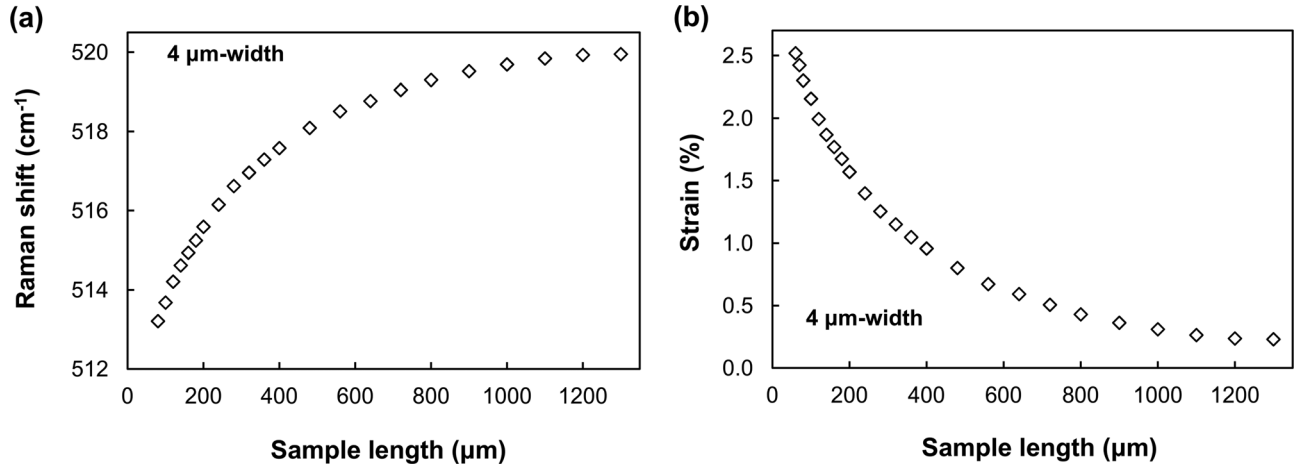

FIG. 10. (a) Variation in Raman peak position for samples with lengths ranging from 60 to 1300 μm. (b) Strain values for the same samples after conversion from Raman shifts.

et al. (Fig. 10(b)).[47] For uniaxial stress along the [110] direction, the relation between Raman shift and strain is given by

$$\Delta\omega = 337\,\varepsilon, \tag{6}$$

where $\Delta\omega$ represents the difference between the stress free frequency value $\omega_0 = 520.7\,\mathrm{cm}^{-1}$ and that measured with applied stress. Figure 11 compares experimental values of strain (determined by SEM and Raman spectroscopy) and strain determined analytically for the 1 and 2 μm-wide samples. The average discrepancy for the range of lengths is found to be ~0.05% strain (equivalent to 80 MPa stress) between the two experimental techniques and theory. This small error validates the accuracy in conversion from Raman wavenumbers to strain.

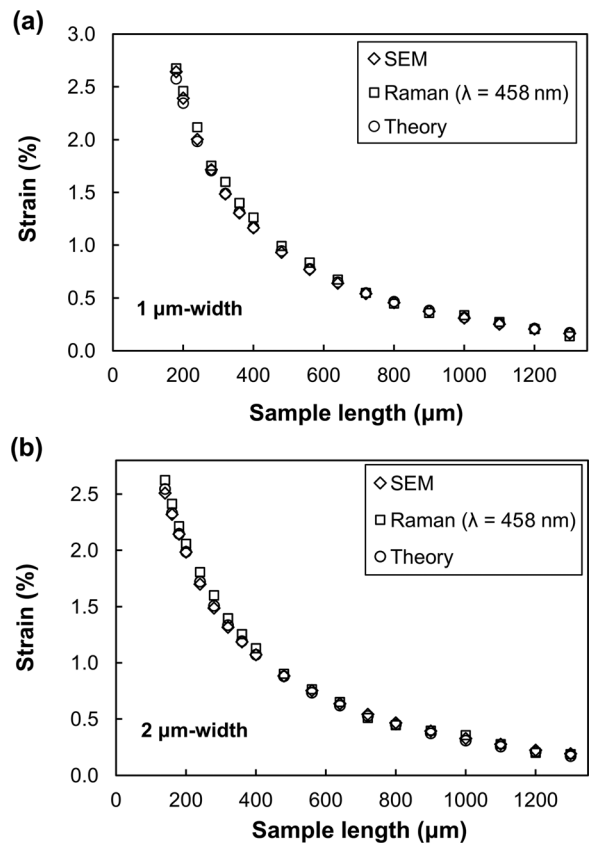

FIG. 11. SEM, Raman measurements, and theory show excellent agreement in strain values for all geometries: (a) 1 μm- and (b) 2 μm-wide samples.

The good agreement obtained between theory and experiments confirms the technique is suitable for accurate analysis of strain in suspended silicon beams, thin films, and nanowires in the range 0–3% (equivalent to a mechanical stress of 5 GPa). This range of values is similar to that used in other experimental work in bulk silicon.[48,49] Kozhusko *et al.*[48] using nonlinear surface acoustic wave (SAW) pulses, measured the critical fracture strength of single crystal silicon and obtained values in the range 5–7 GPa. Ando *et al.*[49] measured the fracture strain in single crystal silicon samples 50 μm-long, 50 μm-wide, and 5 μm-thick along the [110] direction and found an average fracture strain of 3.4%. The ideal tensile strength has also been calculated for a perfect crystal.[50,51] A range of values from 15 to 22 GPa was obtained depending on the stress orientation. However, unlike perfect crystals, real materials contain defects such as impurities, dislocations, and vacancies which reduce the tensile strength. Thus, the ideal tensile strength must be considered as an upper limit for a real material.

Finally, the strain distribution along the silicon sample was investigated. Raman measurements were carried out in three different locations along the sample length; at each end and in the centre. This is in contrast to the previous Raman analysis where each measurement was performed at three locations near the centre of the beam length. Figure 12 shows the Raman spectra for the 4 μm-wide samples. Since no significant differences are observed, it is concluded that strain is homogeneously distributed along the sample length. Strain distribution is particularly important in silicon nanowires where small changes in strain can significantly modify the silicon band gap and electron effective mass m^*.[52,53] Any such changes cause a change in carrier mobility, which affects performance in nanowire based devices. Standard deviations and normality tests with a 95% confidence interval were carried out for the SEM measurements from the

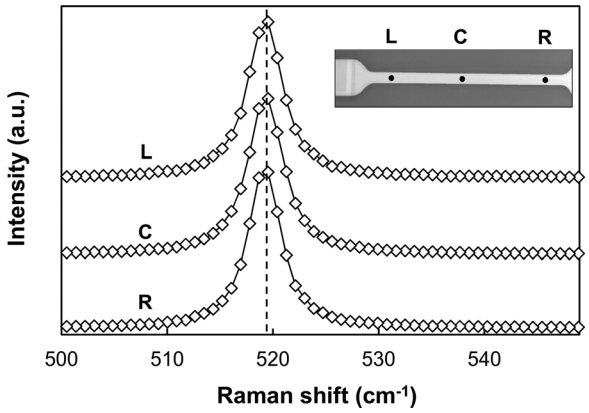

FIG. 12. Raman spectra corresponding to a 4 μm-wide sample in three different locations along the sample length. No difference in peak position was found between the three locations indicating a homogenous strain distribution.

four measured cursor displacements Δu (Fig. 13(a)) and Raman frequency shifts $\Delta\omega$ (Fig. 13(b)). For both types of strain measurement, p-values > 0.05 are obtained which validates the null hypothesis, i.e., a normal distribution. The small standard deviations, $\sigma_{\Delta u} = 0.09603$ and $\sigma_{\Delta\omega} = 0.06345$, confirm good uniformity in both SEM and Raman measurements.

B. Size effects on the silicon mechanical properties

The mechanical properties of silicon such as the Young's modulus and fracture strain have been previously reported and found to be size dependent.[14,15,30,54] Based on our SEM and Raman measurements, we have analyzed the dependence of Young's modulus and fracture strain on beam size and compared the findings with previously reported results.

1. Young's modulus

To analyze the size dependency of the Young's modulus, five arrays of silicon samples with widths between 1 and 4 μm were studied. In order to calculate the Young's modulus, we first determine the applied stress using Eq. (3), which can be written as

$$\sigma = E_a \frac{S_a}{S}\left(\frac{u_{free}}{L_{a0}^{free}} - \frac{u}{L_{a0}}\right). \quad (7)$$

Eq. (7) does not require use of Young's modulus in silicon. The Young's modulus of the sample can be subsequently

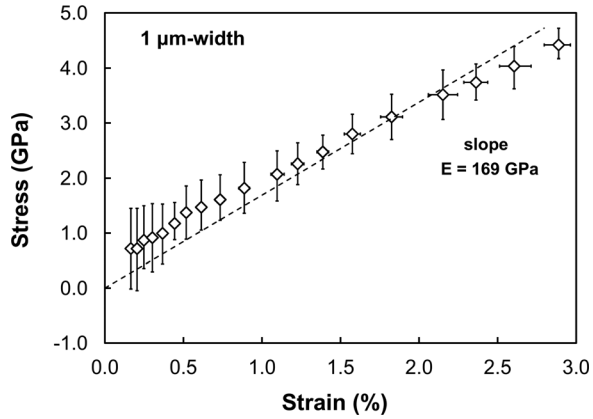

FIG. 14. The stress–strain curve for a sample and weighted linear fitting (dashed line). Stress and strain are both determined from SEM measurements. The fitted line is drawn assuming a zero sample mismatch strain and residual stress and crosses over the region of maximum cursor displacement (minimum Young's modulus fluctuation). The Young's modulus is extracted from the slope of the fitted line.

extracted from the slope of the stress-strain curve by applying a least squares linear fit. The main error in stress and strain determination, hence in Young's modulus, results as a consequence of the cursor displacement variations. To minimize the error in Young's modulus determination, the fitted line is drawn to span over the region where the cursor displacement variations is minimum. The analysis of the first derivative of the Young's modulus with respect to the cursor displacement shows that the region where the Young's modulus is less prone to fluctuations occurs around the maximum of the cursor displacement curve (Fig. 6). In addition, the constriction of zero mismatch strain and residual stress forces the fitted line to cross at the origin. Figure 14 shows the stress-strain curve and the fitted line used to extract the Young's modulus for a 1 μm-wide array of samples. The fitted line corresponds to a Young's modulus of 169 GPa.

The average Young's modulus for the five arrays of samples was found to be 165 GPa and the standard deviation was 5 GPa. Thus, within the accuracy of the SEM measurements, our results confirm that the Young's modulus of the samples is similar to that of bulk silicon, i.e., 169 GPa. These results are summarized in Table I.

The Young's modulus of 200 nm-thick silicon freestanding beams was previously determined using dynamic resonance-based measurements.[55] An average value of ~160 GPa was found, which is within 5% of the bulk value.

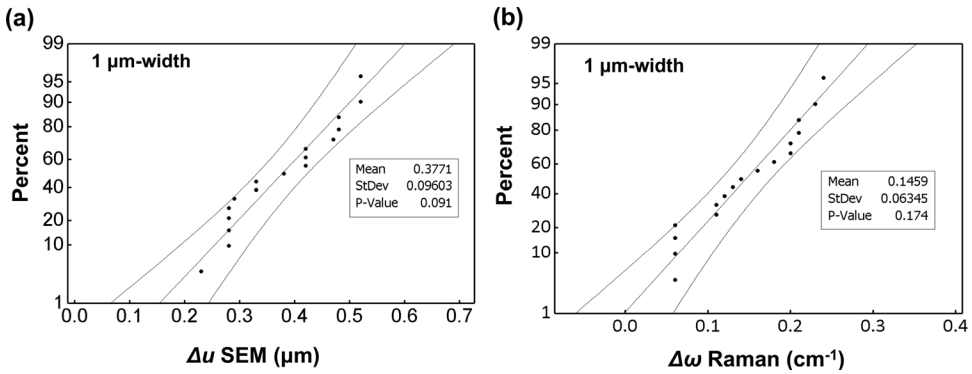

FIG. 13. Normality tests with 95% confidence intervals of (a) SEM discrepancies of displacement u for 1 μm-wide samples corresponding to the four cursors measurements per sample, (b) Raman discrepancies in frequency shifts for samples corresponding to three measurement locations per sample. P-values > 0.05 validated a normality distribution in both sets of measurements. Standard deviations are $\sigma_{\Delta u} = 0.09603$ and $\sigma_{\Delta\omega} = 0.06345$.

TABLE I. Experimental Young's modulus extracted using Eqs. (1) and (7).

Sample	A	B	C	D	E
Width (μm)	4	2	2	1	1
Young's modulus (GPa)	166	171	161	160	169
Average (GPa)			165		
Standard deviation (GPa)			5		

This result is slightly smaller than the present findings obtained by SEM. Discrepancies in Young's modulus evaluated using different techniques have previously been reported. Jin *et al.*[56] compared different techniques to extract the Young's modulus including resonance, electrostatic pull-in, SEM, and TEM. They observed a general decrease in Young's modulus with decreasing nanobeam thickness, although the onset of the reduction in Young's modulus occurred at higher thicknesses for the resonance and pull-in methods compared with SEM and TEM. A decreasing trend in Young's modulus with decreasing thickness has also previously been reported.[57] Other groups, however, have found no Young's modulus size-dependency,[25,58,59] and in some cases, a Young's modulus increase with decreasing thickness has been reported.[20] Table II compares our measurements with these data. *Ab initio* calculations predict a size dependency in Young's modulus for dimensions below 10 nm.[60,61] Several effects including surface stress,[62,63] native oxide,[64–66] loading conditions,[67] and material defects[15,68] are believed to affect the Young's modulus and mechanical properties in general. Nevertheless, none of them can individually explain all the differences observed between various experiments and theory. Sadeghian *et al.*[15] used molecular dynamics simulations to study the size-dependent elasticity of silicon nanocantilevers and concluded that the differences between experiments and theory could be reduced if surface effects, native oxide layers, and fabrication-induced defects were included in the simulation.

2. Fracture strain

In order to study the effect of structure dimensions on fracture strain, forty arrays of thirty samples, each with different geometries, were studied. Fracture strain was analyzed by visual inspection of the last unbroken sample within each array.

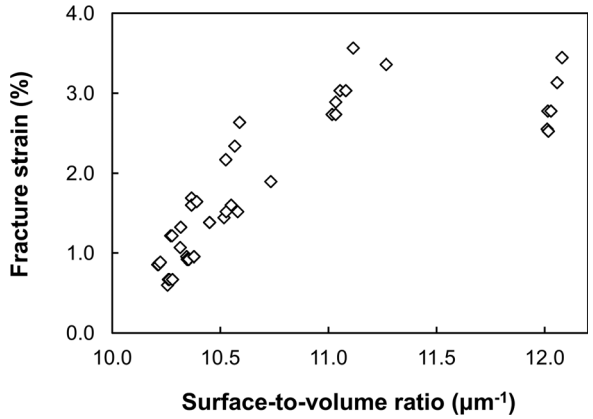

FIG. 15. The dependence of fracture strain on the surface-to-volume ratio. The increase in fracture strain with increasing surface-to-volume ratio appears to flatten at the highest ratios.

For the 1 μm-wide nanowires, 3.6% strain corresponding to ~6 GPa (assuming $E = 169$ GPa) stress was obtained. This value is in good agreement with previous experiments in silicon nanowires with similar dimensions along the [110] direction.[30]

Figure 15 shows the dependence of fracture strain on surface-to-volume ratio, calculated from the sample geometry. The data show that fracture strain increases with increasing surface-to-volume ratio, although this tendency seems to stabilize at the highest surface-to-volume ratios. An analysis of samples with smaller dimensions would confirm that the general increasing trend is also preserved at high surface-to-volume ratios. Figure 16 shows the same relationship for samples having the same actuator widths but different sample widths. There is a 2% increase in fracture strain (from around 1% to 3%) as the sample width is reduced from 10 μm to 1 μm. These results agree with other recent studies of the fracture strain in silicon.[30,67] Steighner *et al.*[30] investigated the size-dependence of silicon nanowire strength under tensile stress. Nanowires with diameters ranging from 268 to 840 nm and with different orientations were studied, and fracture strain was found to decrease with increasing diameter. The magnitude of the change was further dependent on crystal orientation. Tang *et al.*[67] studied the fracture mechanisms of silicon nanowires grown along the [111] direction with diameters ranging from 9 to 42 nm. Under tension, the silicon nanowires deformed elastically before exhibiting an

TABLE II. Comparison of Young's modulus extracted using different methods.

Work	Method	Loading	Orientation	Young's modulus(GPa)
Li *et al.*[a]	Resonance	Bending	110	142
Gordon *et al.*[b]	AFM force modulation and tapping	Bending	111	100, 140, 185
Sadeghian *et al.*[c]	Electrostatic pull-in instability	Bending	110	161
Sohn *et al.*[d]	AFM indentation	-	111	70–240
	Static SEM cursor displacement	Tensile	110	165
Our work	Dynamic resonant methods	Tensile	110	160

[a]Ref. 14, Young's modulus is extracted by cubic interpolation from the supplied data for a thickness of 200 nm.
[b]Ref. 20, selected results for vapor-liquid-solid grown nanowires with diameters of 700, 480, and 450 nm, respectively.
[c]Ref. 57, Young's modulus is extracted by cubic interpolation from the supplied data for a thickness of 200 nm.
[d]Ref. 58, chemically grown nanowires with diameters between 80–600 nm.

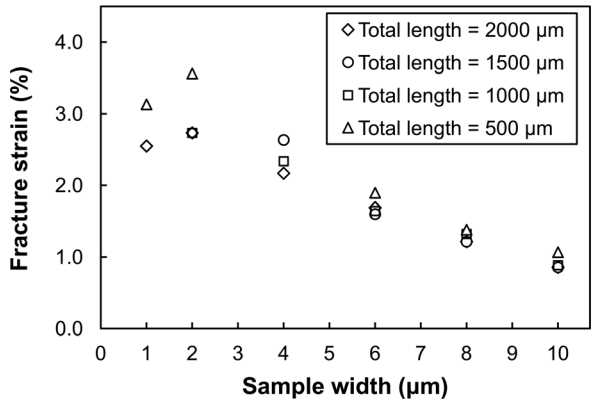

FIG. 16. The dependence of fracture strain on the sample width. There is an increase in fracture strain with reducing sample width.

abrupt brittle fracture, and again there was an increase in tensile strength with decreasing diameter. However, under bending they observed that the silicon nanowires deformed plastically.[67]

Fracture mechanisms in crystals are complex and have been studied both experimentally and theoretically.[30,48,67,69–71] The fracture process is frequently initiated at a flaw or at a surface defect.[69,71] Since defects are usually randomly distributed,[30] there is a decreased probability of defects in smaller structures.[30,67] This could explain the increase in fracture strain with decreasing size. However, other factors such as inhomogeneous defect distributions are also believed to affect the fracture strain of brittle materials such as polycrystalline silicon.[72] Previous work on polycrystalline silicon, based on Weibull analysis, predicts the fracture originates on the edges, corners, and surface of the specimens.[73,74] Weibull failure analysis is usually employed to study the fracture of brittle materials based on the weakest link hypothesis (worst flaw).[75] The validity of the Weibull analysis, however, has been questioned at the micrometer scale.[75,76] There is little information on the impact of the defects distribution in silicon nanowires under tensile stress, but it is possible that this may also play a role in the variation in fracture strain observed here.

C. Surface effects

Surface effects such as surface stress, contamination, and native oxide can affect the mechanical properties of the material.[62,66,77] The surface stress is the reversible work per unit area required to stretch a surface elastically.[78] It originates from the reconstruction, relaxation, and molecular adsorption of atoms on the surface.[62,64,77] Sadeghian *et al.*[62] studied the effect of changes in the stiffness of silicon cantilevers on their resonance frequency in air and vacuum due to surface stress. They observed that when the cantilever dimensions approach the nanometric regime, the change in resonance frequency due to surface stress becomes significant. Zang *et al.*[77] studied the effect of molecular adsorption on the bending of nanocantilevers and observed that their behavior significantly differs compared with microscopic and macroscopic thick cantilevers. The work shows that the classical Stoney's equation used to calculate the bending curvature required modification when the thickness of cantilevers is reduced to a few nanometers.

Native oxide can also affect the mechanical properties of silicon nanowires. The smaller Young's modulus of SiO_2 (~73 GPa[20,79]) compared with silicon and the thickness of the native oxide layer itself (2–5 nm[64]) are contributing factors to the observed changes to the Young's modulus in nanowires.[64,65]

In order to study the impact of surface effects in the structures, we have compared the Raman spectra obtained using the visible and UV lasers, since the signal from the visible laser primarily probes the bulk whereas the UV laser provides information nearest to the surface. Figure 17 shows the strain for the 4 μm-wide samples having lengths in the range 60 – 1300 μm. Only minor discrepancies of ~0.05% strain between the two radiations are found across the entire range of strains (~0 to 2.6%). For the 2 and 1 μm-wide samples, the discrepancies are slightly larger, 0.10% and 0.16%, respectively. Both lasers have penetration depths significantly larger than the thickness of the native oxide layer and both lasers are optically transparent in silicon dioxide. Therefore, additional factors other than surface effects alone must contribute to the discrepancies in strain determined using the two lasers. For example, additional heating from the UV laser heating may play a role. This is discussed in Sec. III D.

D. Thermal conductivity

Previous work on the thermal conductivity of solids and liquids, including some covalent semiconductors under pressure,[80] concluded that thermal conductivity increases in semiconductors with compressive strain, aside from a small decrease observed in silicon under uniaxial stress. Similar results were found through molecular-dynamics simulations in diamond films[81] and more recently in silicon nanowires and thin films.[82] In general, these studies agree on two factors; first that stress-induced defects, which increase phonon scattering, dominate thermal conductivity, and second, that the overall thermal conductivity continually decreases as the applied strain changes from compressive to tensile. Gan

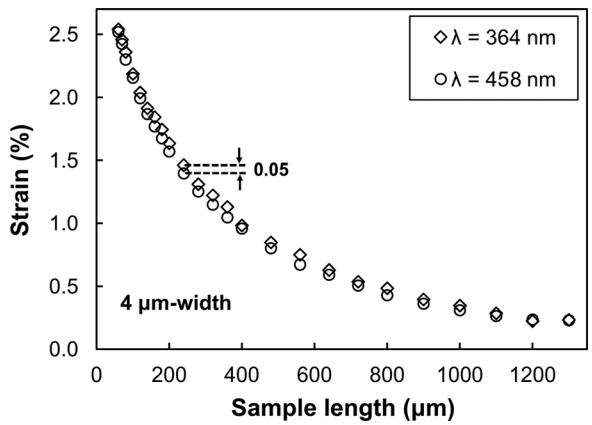

FIG. 17. The strain determined by Raman measurements using UV and visible radiations. There is good agreement in strain values across the entire range of strains and geometries. Since the UV radiation probes only ~ 15 nm while the visible radiation probes the whole sample thickness (200 nm), the data suggest that strain is homogenous throughout the structures.

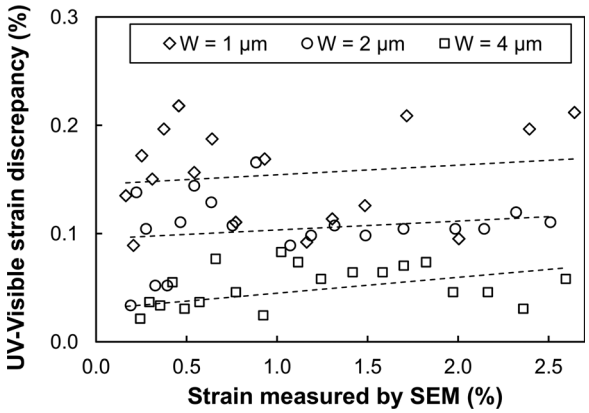

FIG. 18. The variation in strain discrepancy (between UV and visible Raman measurements) with induced strain (measured with SEM). A slight increase in discrepancies with strain is observed (slope of dotted lines). However, the significant scatter in data suggests that other factors such as laser heating have to be considered.

et al.[83] investigated the thermal conductivity change with strain in heavily doped silicon cantilevers with dimensions of $225 \times 42 \times 5\ \mu m^3$ and found that the thermal conductivity increases from 110 to $140\ Wm^{-1}K^{-1}$ when the compressive strain increases from 0.1 to 0.3%. Other factors such as surface stress,[84] geometry,[82] and defects[85] are also shown to affect the thermal conductivity of nanostructures.

In order to investigate changes in thermal conductivity with strain, we have used the discrepancy in the UV-visible Raman shift of the nanostructures as a measure of heat evacuation. Figure 18 shows the variation in UV-visible measurements with strain determined by SEM. For the data acquisition, the UV and visible laser powers are kept constant. Therefore, any significant change in UV-visible discrepancy could indicate a change in heat evacuation related to the thermal conductivity. However, only a slight increase in discrepancy with strain is observed (highlighted by the dotted lines) and the scatter in data is too large to ascribe this to changes in thermal conductivity or surface effects. Consequently, we believe that other factors such as a less effective heat evacuation in samples with smaller dimensions are likely to dominate the results.[86]

IV. SUMMARY AND CONCLUSIONS

Strain has been characterized in arrays of free-standing silicon beams using Raman spectroscopy, SEM measurements, and analytical calculations. The beams were fabricated with a wide range of geometries under uniaxial tensile stress along the [110] direction. The induced strain was varied and controlled by the beam geometry and fabrication process which enabled a large number of structures to be fabricated on the same chip. The beam geometries (1440 in total) comprised six different widths of 1, 2, 4, 6, 8, and 10 μm with lengths varying between 3 and 1300 μm and a constant thickness of 200 nm. SEM and Raman data were converted to strain values and compared with analytical calculations. There is a good agreement between Raman, SEM, and theory. The small average discrepancies in strain between experiment and theory ($\sim$0.05% using Raman and $\sim$0.04% using SEM) confirm that accurate conversion of Raman measurements to strain is possible in the range 0 to 3% strain. The good agreement between characterization techniques also gives validity to the on-chip test structures as a method to produce accurate strain levels in beams over a large range of sample lengths.

The dependency of Young's modulus and fracture strain on beam size has also been studied. Static SEM measurements showed that the Young's modulus of 200 nm-thick samples is close to that of bulk silicon. This result was shown to be slightly higher to that obtained previously with dynamic resonance methods for the same thickness. The discrepancies between the two methods and the variation in the extracted values using SEM measurements (standard deviation = 5 GPa) indicate that the Young's modulus and its determination depends on internal and external factors including surface stress, native oxide, loading conditions, and the measurement technique.

The fracture strain was investigated by visual inspection of the last unbroken sample within forty arrays of thirty samples and values up to 3.6% were identified. The fracture strain was shown to increase with decreasing beam width due to the increased surface-to-volume ratio for smaller widths. The variation in fracture strain with surface-to-volume ratio is considered to arise from a lower probability of defects in smaller structures and the likelihood that fracture originates in material flaws or surface defects. Homogeneity of the defect distribution may also affect the fracture strain.

UV and visible lasers having penetration depths of 15 nm and 300 nm in silicon, respectively, were used to study the role of the surface on the size dependent material properties. Small discrepancies in Raman shift between the two lasers were attributed to a small increase in sample heating using the UV laser. The variation of thermal conductivity with tensile strain was thus investigated using the discrepancy between Raman measurements as a measure of heat evacuation. Within the range of strain studied (0–3%) and limited by the scatter in the data, a small decrease in thermal conductivity was found for the most tensile strained samples compared with bulk silicon.

ACKNOWLEDGMENTS

The authors would like to acknowledge the financial support from the Engineering and Physical Sciences Research Council (EPSRC).

[1]Y. Cui, Q. Wei, H. Park, and C. M. Lieber, Science **293**(5533), 1289–1292 (2001).
[2]V. Passi, F. Ravaux, E. Dubois, S. Clavaguera, A. Carella, C. Celle, J. P. Simonato, L. Silvestri, S. Reggiani, D. Vuillaume, and J. P. Raskin, IEEE Electron Device Lett. **32**(7), 976–978 (2011).
[3]X. T. Zhou, J. Q. Hu, C. P. Li, D. D. D. Ma, C. S. Lee, and S. T. Lee, Chem. Phys. Lett. **369**(1–2), 220–224 (2003).
[4]N. Singh, A. Agarwal, L. K. Bera, T. Y. Liow, R. Yang, S. C. Rustagi, C. H. Tung, R. Kumar, G. Q. Lo, N. Balasubramanian, and D. L. Kwong, IEEE Electron Device Lett. **27**(5), 383–386 (2006).
[5]R. Wang, H. Liu, R. Huang, J. Zhuge, L. Zhang, D. W. Kim, X. Zhang, D. Park, and Y. Wang, IEEE Trans. Electron Devices **55**(11), 2960–2967 (2008).

[6]A. A. Barlian, W. T. Park, J. R. Mallon, Jr., A. J. Rastegar, and B. L. Pruitt, Proc. IEEE **97**(3), 513–552 (2009).
[7]M. Chu, Y. K. Sun, U. Aghoram, and S. E. Thompson, Annu. Rev. Mater. Res. (Annual Reviews, Palo Alto) **39**, 203–229 (2009).
[8]T. A. Langdo, M. T. Currie, Z. Y. Cheng, J. G. Fiorenza, M. Erdtmann, G. Braithwaite, C. W. Leitz, C. J. Vineis, J. A. Carlin, A. Lochtefeld, M. T. Bulsara, I. Lauer, D. A. Antoniadis, and M. Somerville, Solid-State Electron. **48**(8), 1357–1367 (2004).
[9]S. E. Thompson, G. Sun, Y. S. Choi, and T. Nishida, IEEE Trans. Electron Devices **53**(5), 1010–1020 (2006).
[10]R. Degraeve, G. Groeseneken, I. De Wolf, and H. E. Macs, IEEE Trans. Electron Devices **44**(6), 943–950 (1997).
[11]S. M. Hu, J. Appl. Phys. **70**(6), R53–R80 (1991).
[12]R. Hull, *Properties of Crystalline Silicon* (Institution of Engineering and Technology).
[13]X. Han, K. Zheng, Y. Zhang, X. Zhang, Z. Zhang, and Z. L. Wang, Adv. Mater. **19**(16), 2112–2118 (2007).
[14]X. Li, T. Ono, Y. Wang, and M. Esashi, Appl. Phys. Lett. **83**(15), 3081–3083 (2003).
[15]H. Sadeghian, H. Goosen, A. Bossche, B. Thijsse, and F. Van Keulen, J. Phys. D **44**(7), 072001 (2011).
[16]L. B. Freund and S. Suresh, *Thin Film Materials: Stress, Defect Formation, and Surface Evolution* (Cambridge University Press, Cambridge, England, New York, 2003).
[17]H. Ibach, Surf. Sci. Rep. **29**(5–6), 195–263 (1997).
[18]I. Ponomareva, D. Srivastava, and M. Menon, Nano Lett. **7**(5), 1155–1159 (2007).
[19]H. Sadeghian, J. F. L. Goosen, A. Bossche, B. J. Thijsse, and F. van Keulen, Thin Solid Films **518**(12), 3273–3275 (2010).
[20]M. J. Gordon, T. Baron, F. Dhalluin, P. Gentile, and P. Ferret, Nano Lett. **9**(2), 525–529 (2009).
[21]G. Y. Jing, H. L. Duan, X. M. Sun, Z. S. Zhang, J. Xu, Y. D. Li, J. X. Wang, and D. P. Yu, Phys. Rev. B **73**, 235409 (2006).
[22]S. Sundararajan and B. Bhushan, Sens. Actuators, A **101**(3), 338–351 (2002).
[23]V. T. Srikar, A. K. Swan, M. S. Ünlü, B. B. Goldberg, and S. M. Spearing, J. Microelectromech. Syst. **12**(6), 779–787 (2003).
[24]S. S. Walavalkar, A. P. Homyk, M. D. Henry, and A. Scherer, J. Appl. Phys. **107**(12), 124314 (2010).
[25]C. L. Hsin, W. Mai, Y. Gu, Y. Gao, C. T. Huang, Y. Liu, L. J. Chen, and Z. L. Wang, Adv. Mater. **20**(20), 3919–3923 (2008).
[26]H. D. Espinosa, Y. Zhu, and N. Moldovan, J. Microelectromech. Syst. **16**(5), 1219–1231 (2007).
[27]M. A. Haque and M. T. A. Saif, Exp. Mech. **42**(1), 123–128 (2002).
[28]S. Lu, Z. Guo, W. Ding, and R. S. Ruoff, Rev. Sci. Instrum. **77**(5), 056103 (2006).
[29]W. Kang, J. H. Han, and M. T. A. Saif, J. Microelectromech. Syst. **19**(6), 1322–1330 (2010).
[30]M. S. Steighner, L. P. Snedeker, B. L. Boyce, K. Gall, D. C. Miller, and C. L. Muhlstein, J. Appl. Phys. **109**(3), 033503 (2011).
[31]Y. Zhang, X. Liu, C. Ru, Y. L. Zhang, L. Dong, and Y. Sun, J. Microelectromech. Syst. **20**(4), 959–967 (2011).
[32]T. Namazu and S. Inoue, Fatigue Fract. Eng. Mater. Struct. **30**(1), 13–20 (2007).
[33]A. Armigliato, R. Balboni, S. Balboni, S. Frabboni, A. Tixier, G. P. Carnevale, P. Colpani, G. Pavia, and A. Marmiroli, Micron **31**(3), 203–209 (2000).
[34]A. Toda, N. Ikarashi, and H. Ono, J. Cryst. Growth **210**(1), 341–345 (2000).
[35]P. Zhang, A. A. Istratov, E. R. Weber, C. Kisielowski, H. He, C. Nelson, and J. C. H. Spence, Appl. Phys. Lett. **89**(16), 161907 (2006).
[36]I. De Wolf, Semicond. Sci. Technol. **11**(2), 139–154 (1996).
[37]S. Gravier, M. Coulombier, A. Safi, N. Andre, A. Boe, J. P. Raskin, and T. Pardoen, J. Microelectromech. Syst. **18**(3), 555–569 (2009).
[38]H. Idrissi, B. Wang, M. S. Colla, J. P. Raskin, D. Schryvers, and T. Pardoen, Adv. Mater. **23**(18), 2119–2122 (2011).
[39]M. S. Colla, B. Wang, H. Idrissi, D. Schryvers, J. P. Raskin, and T. Pardoen, Acta Mater. **60**(4), 1795–1806 (2012).
[40]J. F. Nye, *Physical Properties of Crystals: Their Representation by Tensors and Matrices*, 1st published in pbk. with corrections ed. (Clarendon, Oxford Oxfordshire, 1985).
[41]M. A. Hopcroft, W. D. Nix, and T. W. Kenny, J. Microelectromech. Syst. **19**(2), 229–238 (2010).
[42]K. F. Dombrowski, I. De Wolf, and B. Dietrich, Appl. Phys. Lett. **75**(16), 2450–2451 (1999).
[43]V. Passi, U. Sodervall, B. Nilsson, G. Petersson, M. Hagberg, C. Krzeminski, E. Dubois, B. D. Bois, and J. P. Raskin, Microelectron. Eng. **95**, 83–89 (2012).
[44]A. Boé, A. Safi, M. Coulombier, T. Pardoen, and J. P. Raskin, Thin Solid Films **518**(1), 260–264 (2009).
[45]I. De Wolf, J. Raman Spectrosc. **30**(10), 877–883 (1999).
[46]C. Georgi, M. Hecker, and E. Zschech, J. Appl. Phys. **101**(12), 123104 (2007).
[47]E. Anastassakis, A. Pinczuk, E. Burstein, F. H. Pollak, and M. Cardona, Solid State Commun. **8**(2), 133–138 (1970).
[48]V. V. Kozhushko, A. M. Lomonosov, and P. Hess, Phys. Rev. Lett. **98**(19), 195505 (2007).
[49]T. Ando, M. Shikida, and K. Sato, Sensors Actuators, A **93**(1), 70–75 (2001).
[50]D. Roundy and M. L. Cohen, Phys. Rev. B **64**, 212103 (2001).
[51]Y. Umeno, A. Kushima, T. Kitamura, P. Gumbsch, and J. Li, Phys. Rev. B **72**(16), 165431 (2005).
[52]C. Tuma and A. Curioni, Appl. Phys. Lett. **96**(19), 193106 (2010).
[53]D. Shiri, Y. Kong, A. Buin, and M. P. Anantram, Appl. Phys. Lett. **93**(7), 073114 (2008).
[54]Y. Zhu, F. Xu, G. Qin, W. Y. Fung, and W. Lu, Nano Lett. **9**(11), 3934–3939 (2009).
[55]U. Bhaskar, V. Passi, S. Houri, E. Escobedo–Cousin, S. H. Olsen, T. Pardoen, and J. P. Raskin, J. Mater. Res. **27**(3), 571–579 (2012).
[56]Q. H. Jin, T. Li, Y. L. Wang, X. L. Gao, and F. F. Xu, in Proceedings of the 2010 IEEE Sensors, pp. 2530–2533.
[57]H. Sadeghian, C. K. Yang, J. F. L. Goosen, E. Van Der Drift, A. Bossche, P. J. French, and F. Van Keulen, Appl. Phys. Lett. **94**(22), 221903 (2009).
[58]Y. S. Sohn, J. Park, G. Yoon, J. Song, S. W. Jee, J. H. Lee, S. Na, T. Kwon, and K. Eom, Nanoscale Res. Lett. **5**(1), 211–216 (2010).
[59]A. Heidelberg, L. T. Ngo, B. Wu, M. A. Phillips, S. Sharma, T. I. Kamins, J. E. Sader, and J. J. Boland, Nano Lett. **6**(6), 1101–1106 (2006).
[60]B. Lee and R. E. Rudd, Phys. Rev. B **75**(19), 195328 (2007).
[61]P. W. Leu, A. Svizhenko, and K. Cho, Phys. Rev. B **77**(23), 235305 (2008).
[62]H. Sadeghiant, C. K. Yang, K. B. Gavan, J. F. L. Goosen, E. W. J. M. Van Der Drift, H. S. J. Van Der Zant, P. J. French, A. Bossche, and F. Van Keulen, e-J. Surf. Sci. Nanotechnol. **7**, 161–166 (2009).
[63]H. Yao, G. Yun, N. Bai, and J. Li, J. Appl. Phys. **111**(8), 083506 (2012).
[64]H. Sadeghian, C. K. Yang, J. F. L. Goosen, A. Bossche, U. Staufer, P. J. French, and F. Van Keulen, J. Micromech. Microeng. **20**(6), 064012 (2010).
[65]C. C. Röhlig, M. Niebelschütz, K. Brueckner, K. Tonisch, O. Ambacher, and V. Cimalla, Phys. Status Solidi B **247**(10), 2557–2570 (2010).
[66]J. Wang, Q. A. Huang, and H. Yu, Solid State Commun. **145**(7–8), 351–354 (2008).
[67]D. M. Tang, C. L. Ren, M. S. Wang, X. Wei, N. Kawamoto, C. Liu, Y. Bando, M. Mitome, N. Fukata, and D. Golberg, Nano Lett. **12**(4), 1898–1904 (2012).
[68]H. A. Wu, G. R. Liu, and J. S. Wang, Model. Simul. Mater. Sci. Eng. **12**(2), 225–233 (2004).
[69]A. M. Lomonosov and P. Hess, Phys. Rev. Lett. **89**, 095501 (2002).
[70]S. J. Zhou, P. S. Lomdahl, R. Thomson, and B. L. Holian, Phys. Rev. Lett. **76**(13), 2318–2321 (1996).
[71]G. Lehmann, A. M. Lomonosov, P. Hess, and P. Gumbsch, J. Appl. Phys. **94**(5), 2907–2914 (2003).
[72]E. D. Reedy, B. L. Boyce, J. W. Foulk, R. V. Field, M. P. De Boer, and S. S. Hazra, J. Microelectromech. Syst. **20**(4), 922–932 (2011).
[73]T. Tsuchiya, O. Tabata, J. Sakata, and Y. Taga, J. Microelectromech. Syst. **7**(1), 106–113 (1998).
[74]B. L. Boyce, J. M. Grazier, T. E. Buchheit, and M. J. Shaw, J. Microelectromech. Syst. **16**(2), 179–190 (2007).
[75]O. Borrero–López, M. Hoffman, A. Bendavid, and P. J. Martin, Scr. Mater. **60**(11), 937–940 (2009).
[76]W. N. Sharpe Jr., O. Jadaan, G. M. Beheim, G. D. Quinn, and N. N. Nemeth, J. Microelectromech. Syst. **14**(5), 903–913 (2005).
[77]J. Zang and F. Liu, Nanotechnology **18**(40), 405501 (2007).
[78]R. C. Cammarata and K. Sieradzki, Annu. Rev Mater. Sci. **24**(1), 215–234 (1994).
[79]H. Ni, X. Li, and H. Gao, Appl. Phys. Lett. **88**(4), 043108–043108-3 (2006).
[80]R. G. Ross, P. Andersson, B. Sundqvist, and G. Backstrom, Rep. Prog. Phys. **47**(10), 1347–1402 (1984).

[81]I. Rosenblum, J. Adler, S. Brandon, and A. Hoffman, Phys. Rev. B **62**(4), 2920–2936 (2000).
[82]X. Li, K. Maute, M. L. Dunn, and R. Yang, Phys. Rev. B **81**(24), 245318 (2010).
[83]M. Gan and V. Tomar, Trans ASME J. Eng. Mater. Technol. **133**(4), 041013 (2011).
[84]M. Liangruksa and I. K. Puri, J. Appl. Phys. **109**(11), 113501 (2011).
[85]T. M. Gibbons, B. Kang, S. K. Estreicher, and C. Carbogno, Phys. Rev. B **84**(3), 035317 (2011).
[86]J. Anaya, A. Torres, A. Martin-Martin, O. Martinez, A. C. Prieto, J. Jimenez, A. Rodriguez, J. Sangrador, and T. Rodriguez, in *Vi Encuentro Franco-Espanol De Quimica Y Fisica Del Estado Solido - Vi Rencontre Franco-Espagnole Sur La Chimie Et La Physique De L Etat Solide*, edited by J. J. A. M. D. F. Carvajal (2010), Vol. 8, pp. 78–83.